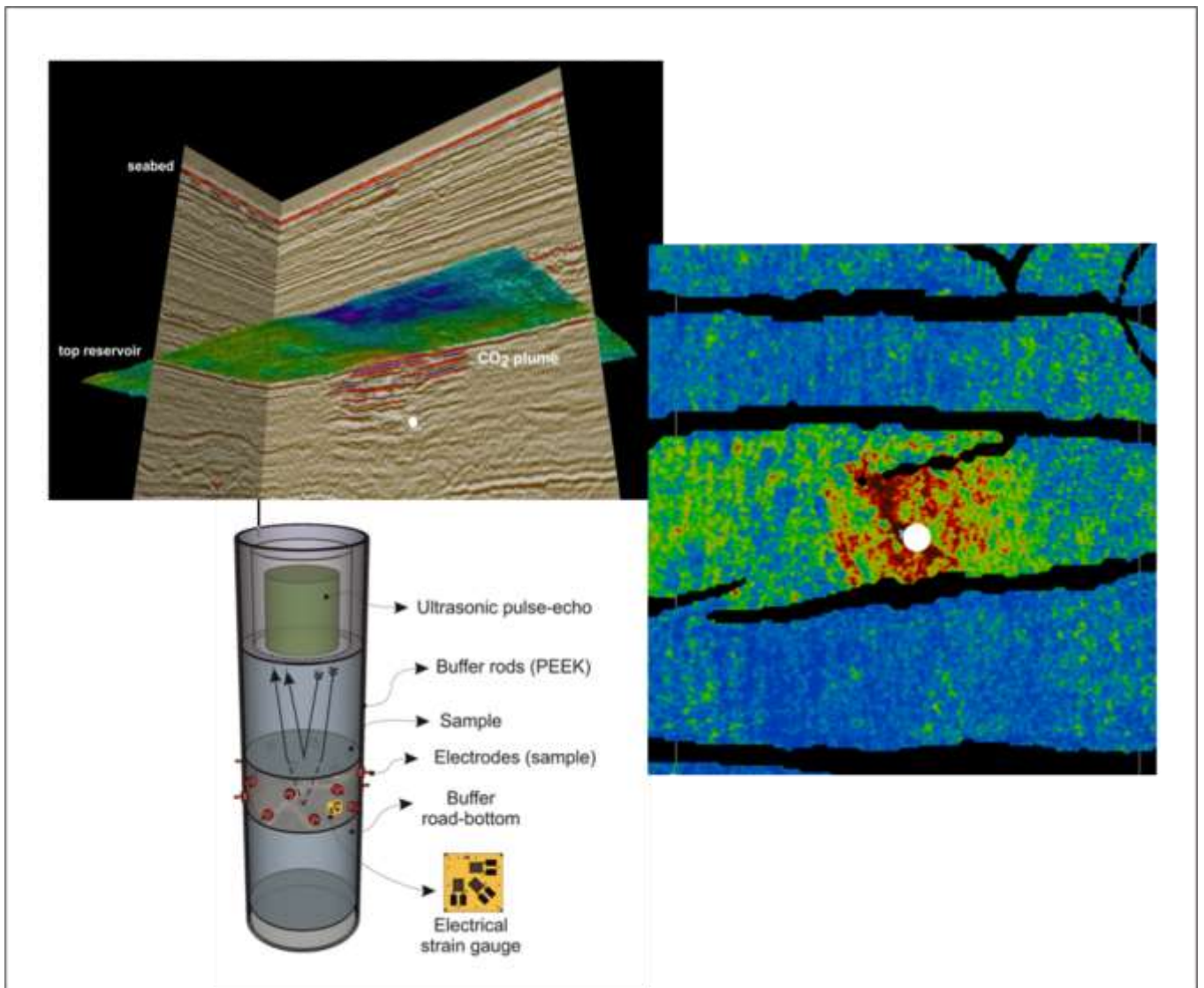# DiSECCS - Diagnostic Seismic Toolbox for Efficient Control of CO₂ Storage

Work Package 5 - Seismic Analysis Toolbox

BGS Energy Programme Report OR/17/013

BRITISH GEOLOGICAL SURVEY

ENERGY PROGRAMME REPORT OR/17/013

DiSECCS Work Package 5 – Seismic Analysis Toolbox

Keyworth, Nottingham   British Geological Survey   2017

BRITISH GEOLOGICAL SURVEY

The full range of our publications is available from BGS shops at Nottingham, Edinburgh, London and Cardiff (Welsh publications only) see contact details below or shop online at www.geologyshop.com

The London Information Office also maintains a reference collection of BGS publications, including maps, for consultation. We publish an annual catalogue of our maps and other publications; this catalogue is available online or from any of the BGS shops.

The British Geological Survey carries out the geological survey of Great Britain and Northern Ireland (the latter as an agency service for the government of Northern Ireland), and of the surrounding continental shelf, as well as basic research projects. It also undertakes programmes of technical aid in geology in developing countries.

The British Geological Survey is a component body of the Natural Environment Research Council.

British Geological Survey offices

BGS Central Enquiries Desk

Tel 0115 936 3143   Fax 0115 936 3276
email enquiries@bgs.ac.uk

Environmental Science Centre, Keyworth, Nottingham NG12 5GG

Tel 0115 936 3241   Fax 0115 936 3488
email sales@bgs.ac.uk

The Lyell Centre, Research Avenue South, Edinburgh EH14 4AP

Tel 0131 667 1000   Fax 0131 668 2683
email scotsales@bgs.ac.uk

Natural History Museum, Cromwell Road, London SW7 5BD

Tel 020 7589 4090   Fax 020 7584 8270
Tel 020 7942 5344/45   email bgslondon@bgs.ac.uk

Columbus House, Greenmeadow Springs, Tongwynlais, Cardiff CF15 7NE

Tel 029 2052 1962   Fax 029 2052 1963

Maclean Building, Crowmarsh Gifford, Wallingford OX10 8BB

Tel 01491 838800   Fax 01491 692345

Geological Survey of Northern Ireland, Colby House, Stranmillis Court, Belfast BT9 5BF

Tel 028 9038 8462   Fax 028 9038 8461
www.bgs.ac.uk/gsni/

Parent Body
Natural Environment Research Council, Polaris House, North Star Avenue, Swindon SN2 1EU

Tel 01793 411500   Fax 01793 411501
www.nerc.ac.uk

Website www.bgs.ac.uk
Shop online at www.geologyshop.com

Foreword

This document comprises a toolbox of seismic software developed and utilised in the project, presented in a form that other practitioners can utilise and tailor to their own specific needs.

Acknowledgements

Contents

Executive Summary

The DiSECCS project (<u>Di</u>agnostic <u>S</u>eismic Toolbox for <u>E</u>fficient <u>C</u>ontrol of <u>C</u>O$_2$ <u>S</u>torage) has developed seismic monitoring tools and methodologies to identify and characterise injection-induced changes, whether of fluid saturation or pressure, in storage reservoirs.
This DiSECCS deliverable comprises a toolbox of seismic software developed and utilised in the project. The tools include software for the measurement and characterisation of thin CO_2 layers by spectral and attenuation analysis, fracture characterisation via wavelet coda analysis, novel rock physics algorithms and a summary of new laboratory analyses.

Full copies of the software codes for practitioners are available to download online.

Background information and further results from DiSECCS can be found on the project website
https://www.bgs.ac.uk/diseccs/

1 Introduction

The DiSECCS seismic analysis toolbox comprises a series of codes which implement various algorithms for analysing post-stack seismic data acquired as part of a geological carbon sequestration monitoring programme. The tools focus on determining the thickness, saturation distribution and physical properties of CO_2 layers imaged on seismic data and are described in detail within this document. A number of new rock physics models have also been developed as part of the DiSECCS project and these are included in the toolbox as a series of *Mathematica* notebooks.

1.1   INSTALLING THE DISECCS SEISMIC UNIX TOOLBOX

To use the spectral decomposition and Q estimation codes included in the toolbox, the Centre for Wave Phenomena Seismic Unix package (CWPSU) from Colorado School of Mines must also be installed. Seismic Unix can be downloaded from http://www.cwp.mines.edu/cwpcodes/ and compiled on any UNIX-like operating system with working C and FORTRAN-90 compilers. Seismic Unix can also be installed under CYGWIN on a windows based system. To install the codes the user must first set two environment variables pointing to the top-level directory(s) containing the Seismic Unix distribution and DiSECCS toolkit (Box 1.1).

```
Using the BASH shell:
export CWPROOT=path_to_seismic_unix_install_dir
export DSUROOT=path_to_diseccs_seismic_unix_install_dir
Using the C shell:
setenv CWPROOT path_to_seismic_unix_install_dir
setenv DSUROOT path_to_diseccs_seismic_unix_install_dir
```

Box 1.1 Setting the environmental variables.

The codes can then be built by modifying $DSUROOT/src/Makefile.config and running make at the top level of the source tree.

2 Spectral decomposition using the Wigner-Ville transform

2.1 BACKGROUND

A key property of a thin (a few metres thick) layer of CO_2, migrating in a storage reservoir, is its temporal thickness, which can be combined with layer velocity to obtain the true layer thickness. If the layer lies beneath the limit of seismic resolution, its temporal thickness cannot be measured directly. Fortunately, tuning effects from such a thin layer produce amplitude and frequency modulation which are diagnostic of temporal thickness. The frequency signature is particularly useful in this respect because it is independent of the acoustic impedance contrasts at the layer interfaces. In order to extract frequency (spectral) information from the reflections associated with individual layers of CO_2, it is necessary to analyse narrow travel-time windows (e.g. 25 ms or less in the Sleipner plume). Conventional linear time-frequency analysis techniques such as the Windowed Fourier Transform suffer from resolution problems - a narrow analysis window localizes the spectrum in time but provides poor frequency resolution, whereas a broader window loses temporal accuracy. The Wigner-Ville Distribution (Wigner 1932; Ville 1948) can potentially overcome some of the limitations inherent in these techniques. The improved resolution offered by the Wigner transform makes it particularly suitable for determining the temporal thickness of individual layers which can only be satisfactorily isolated using a short time window.

2.2 THEORY

The Wigner-Ville Distribution (WVD) function is calculated by computing the power spectrum of a signal (the Fourier transform of the wavelet auto-correlation function) and removing the integration over time (Equation 1). In effect the WVD is constructed by computing the auto-correlation over all possible lags at each time sample (the local auto-correlation function) and transforming into Fourier space:

$$W_{x(t,\nu)} = \int_{-\infty}^{+\infty} X\left(t + \frac{\tau}{2}\right) X*\left(t - \frac{\tau}{2}\right) e^{-i2\pi\nu\tau} d\tau$$

Equation 1

Where W_x is the Wigner-Ville distribution of a function x, t is time, τ the lag, ν the frequency and * represents complex conjugation.

The result is a quadratic function. As a consequence of this, discrete events in a time series will produce cross-terms in the time-frequency distribution. The cross-terms can be reduced by smoothing with an appropriate filter kernel along the time g(x-t) and frequency h(τ) axes (Equation 2) to give the Smoothed Pseudo Wigner-Ville Distribution (SPWVD):

$$SPWVD_{x(t,\nu)} = \int_{-\infty}^{+\infty} h(\tau) \int_{-\infty}^{+\infty} g(x - t) X\left(t + \frac{\tau}{2}\right) X*\left(t - \frac{\tau}{2}\right) e^{-i2\pi\nu\tau} d\tau$$

Equation 2

Smoothing leads to reduced resolution in both the time and frequency planes, forcing a trade-off between resolution and interference effects.

2.3   ALGORITHM

1. Sequentially read the seismic trace data from a CWPSU format file and take the Hilbert transform to form the analytic (complex) trace.
2. Loop over the time dimension and form the local autocorrelation of the analytic trace at each time sample.
3. Apply a smoothing kernel to the local autocorrelation function to attenuate cross-terms.
4. Transform the smoothed local autocorrelation function for each time sample into the frequency domain using a Fourier transform.
5. Store the resulting frequency distribution at each time sample in a time-frequency matrix.
6. Write the time-frequency matrix to a CWPSU format file.

2.4   IMPLEMENTATION

The spectral decomposition algorithm(s) described above have been implemented in ANSI C as a plug-in to the freely available Seismic Unix seismic data processing toolkit (http://www.cwp.mines.edu/cwpcodes/).

The following codes are included in the *specdecomp* directory of the DiSECCS toolbox. In each case the input / output data comprises seismic trace(s) in CWPSU format.

1. *dsuwvtfd1*: implements the unsmoothed Wigner-Ville transform for a single trace. Output is a time-frequency gather.
2. *dsuwvtfd2*: implements the unsmoothed Wigner-Ville transform for a series of seismic traces. Output is an iso-frequency seismic section.
3. *dsupwvtfd1*: implements the Wigner-Ville transform smoothed along the time axis for a single trace. Output is a time-frequency gather.
4. *dsupwvtfd2*: implements the Wigner-Ville transform smoothed along the time axis for a series of seismic traces. Output is an iso-frequency seismic section.
5. *dsuspwvtfd1*: implements the Wigner-Ville transform smoothed along the time and frequency axes for a single trace. Output is a time-frequency gather.
6. *dsuspwvtfd2*: implements the Wigner-Ville transform smoothed along the time and frequency axes for a series of seismic traces. Output is an iso-frequency seismic section.

The BASH shell scripts *testSpecDecomp1d.sh* and *testSpecDecomp2d.sh* found in the *test* directory demonstrates the use of these codes.

2.5   EXAMPLE USAGE

Although less popular than the various linear transforms, the SPWVD has been applied to the spectral decomposition of both active and passive seismic signals (Li & Zheng 2008; Wu & Liu 2006; Prieto et al. 2005). Williams & Chadwick (2012) and White et al. (2013) have successfully used the technique to estimate layer thickness in the Sleipner CO_2 plume, by mapping the tuning peak in a short time window using time-lapse 3D seismic data (
Figure *2.1*).
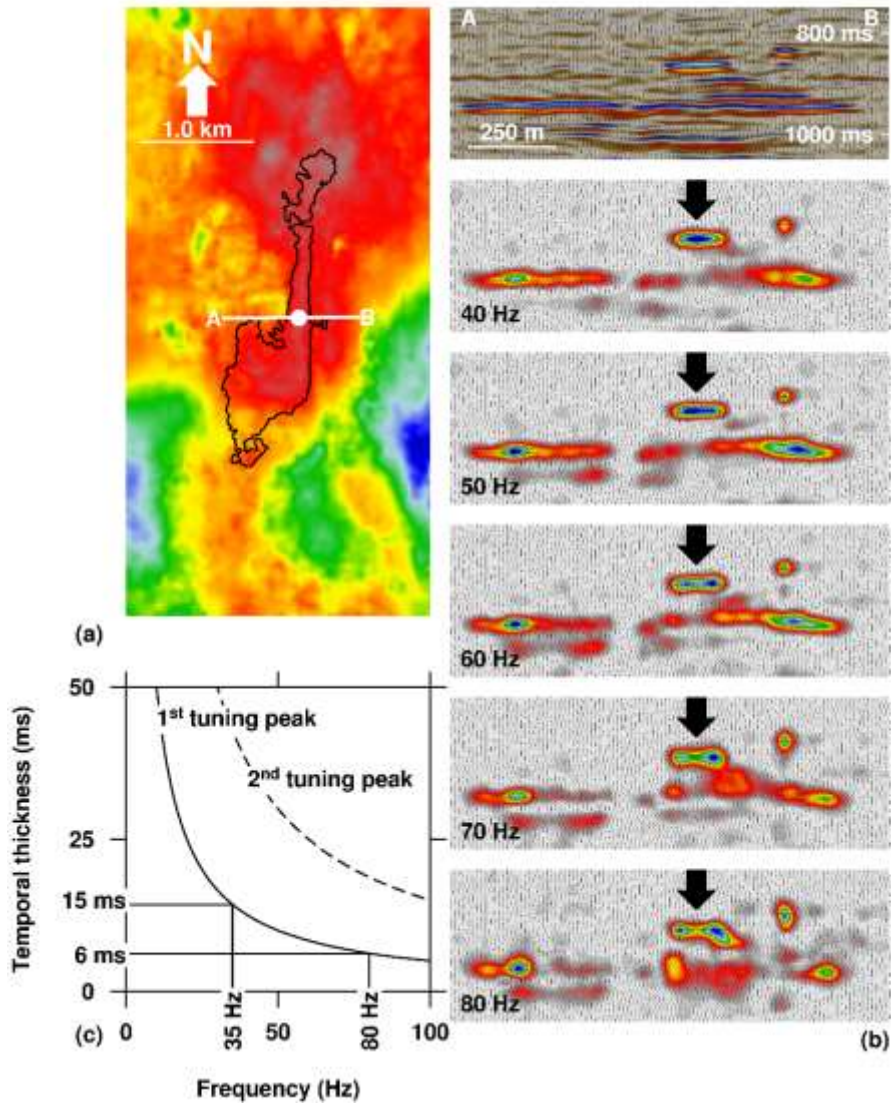
Figure 2.1 Tuning at the southern end of a CO_2-filled ridge beneath the topseal. a) Map view (looking north) of the top of the Utsira reservoir, showing the outer extents of the topmost CO_2 layer in 2006 (black line) and the line of cross-section. b) Discrete frequency slices from the 3D data on a west–east cross-section through the north-trending ridge of CO_2 (computed using the SPWVD with a sliding 24 point Hanning window). Low frequency tuning (~40Hz) occurs along the ridge crest where CO_2 is thickest, with higher frequency tuning (~70 – 80Hz) down the ridge flanks where the CO_2 becomes progressively thinner. c) Tuning curves showing the relationship between frequency and two-way temporal thickness.

A novel use of the SPWVD is presented by White et al. (2015), who discriminated between pressure changes and fluid saturation changes (associated with the CO_2 plume) in the Tubåen storage reservoir at Snøhvit on the basis of 'affected layer' thickness. The CO_2 plume reflectivity (Figure 2.2) is interpreted to come from thin layers of CO_2 tuning at higher frequencies (>25 Hz). Pressure-induced reflectivity is more laterally extensive and characterised by changes in seismic properties which affect the full reservoir thickness with tuning at lower frequencies (<25 Hz).
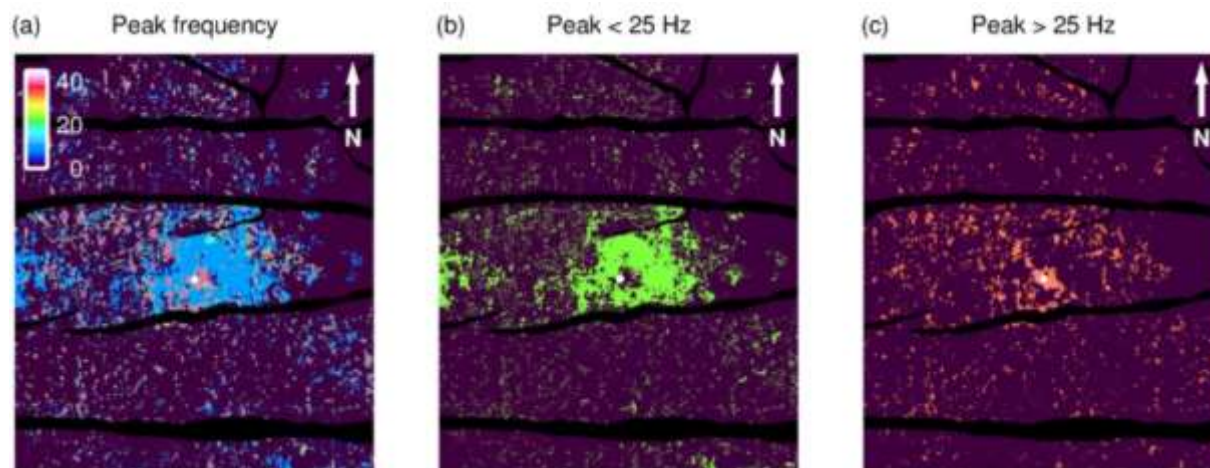
Figure 2.2. Maps of time-lapse changes in the Tubåen storage reservoir at Snøhvit. a) peak tuning frequencies b) tuning frequencies below 25 Hz c) tuning frequencies above 25 Hz. White circle marks CO_2 injection point, black polygons denote faults.

2.6   REFERENCES

Li., Y. & X. Zheng. 2008. Spectral decomposition using Wigner-Ville distribution with applications to carbonate reservoir characterization: The Leading Edge, 27(8), 1050-1057.

Prieto, G. A., Vernon, F.L., Masters, G. & D. J. Thomson. 2005. Multitaper Wigner-Ville Spectrum for Detecting Dispersive Signals from Earthquake Records: Proceedings of the Thirty-Ninth Asilomar Conference on Signals, Systems, and Computers, 938-941.

Ville, J. 1948. Théorie et applications de la notion de signal analytique: Cable Transmission 2A, 61–74.

White, J.C., Williams, G.A. & Chadwick, R.A. 2013. Thin Layer Detectability in a Growing CO_2 Plume: testing the Limits of Time-lapse Seismic Resolution. Energy Procedia 37, 4356–4365. doi:10.1016/j.egypro.2013.06.338.

White, J.C., Williams, G.A., Grude, S. & Chadwick, R.A. 2015. Utilizing spectral decomposition to determine the distribution of injected CO_2 at the Snøhvit Field. Geophysical Prospecting. DOI: 10.1111/1365-2478.12217.

Wigner, E.P. 1932. On the quantum correction for thermodynamic equilibrium: Physical Review, 40, 749–759.

Williams, G. & Chadwick, R.A. 2012. Quantitative seismic analysis of a thin layer of CO_2 in the Sleipner injection plume. Geophysics 77, R245–R256. doi:10.1190/geo2011-0449.1

Wu, X. & Liu, T. 2006. Spectral decomposition of seismic data with reassigned smoothed pseudo Wigner-Ville distribution: Journal of Applied Geophysics, 68, 386-393.

3 Estimation of attenuation using log spectral ratio and peak frequency shift

3.1   BACKGROUND

A key step towards quantifying and understanding the migration of CO_2 in storage reservoirs is to determine the distribution of fluid saturation in the CO_2 layers. This is challenging. When a seismic wave passes through a porous medium it suffers a frequency-dependent attenuation due to the energy loss associated with kinetic interactions of the different fluids (usually water and CO_2) in the pore space. Measurement of the quality factor Q (inverse of the attenuation factor) can provide insights into fluid saturations within the pore-space.

3.2   THEORY

The amplitude spectrum of a wave propagating in an elastic half-space is given by:

$$A(f,t) = A(f)e^{-\frac{\pi f t}{Q}}$$

Equation 3

Where $A(f,t)$ is the amplitude spectrum at time t, $A(f)$ is the amplitude spectrum at time t_0 (the reference spectrum), f is the frequency and Q the Quality factor. Given the travel time (t) it is possible to calculate Q (and hence attenuation) from the spectral variation between two time windows.

3.3   ALGORITHM 1: LOG SPECTRAL RATIO

The most common method is to take the logarithms of the amplitude spectra at two time windows, t_1 and t_2, and fit a linear regression to a plot of the log spectral ratio (LSR) as a function of frequency (Equation 4). The slope (p) of the regression fit is a function of Q and can be used to estimate attenuation using Equation 5.

$$\ln\left[\frac{A(f,t_2)}{A(f,t_1)}\right] = -\frac{\pi f}{Q}(t_2 - t_1)$$

Equation 4

$$Q = -\frac{\pi(t_2 - t_1)}{p}$$

Equation 5

1. Sequentially read the seismic trace data from a CWPSU format file.
2. Window the trace data about the first travel time pick.
3. Form the amplitude spectrum of the windowed data using a Fourier transform.

4. Window the trace data about the second travel time pick.
5. Form the amplitude spectrum of the windowed data using a Fourier transform.
6. Compute the logarithm of the ratio of spectra 1 and 2.
7. Fit a linear function of the form $y=pf+T$ to a selected portion of the frequency spectrum
8. Compute the intercept (T) and gradient (p) of the linear regression. The intercept (T) represents the transmission loss, whilst the gradient (p) can be used to calculate Q from Equation 5.

3.4   ALGORITHM 2: PEAK FREQUENCY SHIFT

An alternative technique uses the relationship between Q and the shift in peak frequency of the source wavelet as it propagates through the earth. Zhang & Ulrychz (2002) derived an expression for Q by assuming that the amplitude spectrum of the initial source wavelet is approximated by a Ricker wavelet. If the peak frequencies at times t_1 and t_2 are fp_1 and fp_2 respectively, then it is possible to calculate Q from:

$$Q = \frac{\pi t_2 fp_2 fm^2}{2\left(fm^2 - fp_2^2\right)}$$

Equation 6a

Where the dominant frequency (fm) is given by:

$$fm = \sqrt{\frac{fp_1 fp_2 (t_2 fp_1 - t_1 fp_2)}{t_2 fp_2 - t_1 fp_1}}$$

Equation 6b

1. Sequentially read the seismic trace data from a CWPSU format file Window trace data about the first travel time pick.
2. Form the amplitude spectrum of the windowed data using a Fourier transform.
3. Compute the peak frequency of the windowed amplitude spectrum.
4. Window trace data about the second travel time pick.
5. Form the amplitude spectrum of the windowed data using a Fourier transform.
6. Compute the peak frequency of the windowed amplitude spectrum.
7. Compute the dominant frequency using Equation 6b.
8. Calculate Q using the shift in peak frequency between the two windowed amplitude spectra according to Equation 6a.

3.5   IMPLEMENTATION

The Q estimation algorithms described above have been implemented in ANSI C as a plug-in to the freely available Seismic Unix seismic data processing toolkit (http://www.cwp.mines.edu/cwpcodes/). The following codes are included in the *qest* directory of

the DiSECCS toolbox. In each case the input / output data comprises seismic trace(s) in CWPSU format.

1. *dsusynqtrace*: generates a synthetic seismic trace of known Q on which to test Q estimation algorithms.
2. *dsuqest*: calculates Q using both the log spectral ratio and peak frequency shift methods.

The BASH shell script *testQSyn.sh* found in the *test* directory demonstrates the use of these codes.

3.6   EXAMPLE USAGE

3.6.1   Synthetic data examples

A synthetic seismic trace comprising two reflections of opposite polarity (Figure 3.1), has a temporal separation of 1 second two-way travel time between the reflection events. The reflectivity spikes have been convolved with a minimum phase wavelet with a dominant frequency of 35 Hz. The resulting stationary seismic trace is shown as a blue curve (Figure 3.1), while the red trace shows the same reflectivity signature, subject to attenuation at a constant Q of 60.
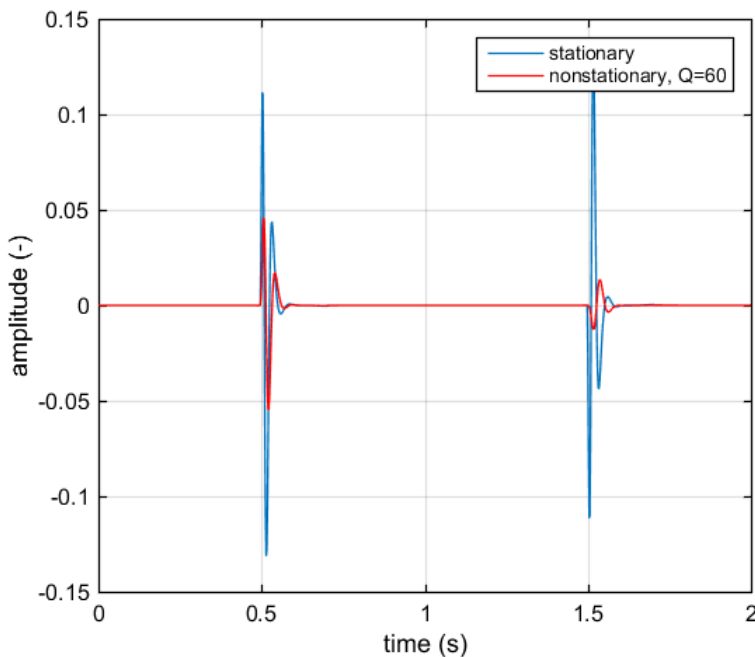
Figure 3.1. Stationary seismic trace (blue curve) calculated by convolving two reflectivity spikes of constant magnitude but opposite polarity with a minimum phase wavelet of dominant frequency 35 Hz. The red curve shows the same reflectivity series subject to attenuation at a constant Q of 60.

Amplitude spectra computed for a time window of 0.2 seconds about the upper and lower reflections are shown in Figure 3.2, with a plot of the log10 of the ratio of both spectra in Figure 3.3. A linear regression (red line) has been fitted to the frequency range 0-70 Hz (Figure 3.3). The slope of this line can be used to compute Q (Equation 5), giving a value of 59.68 for this synthetic noise free example. The peak frequency shift method also predicts the correct Q of 60 for this ideal synthetic case.
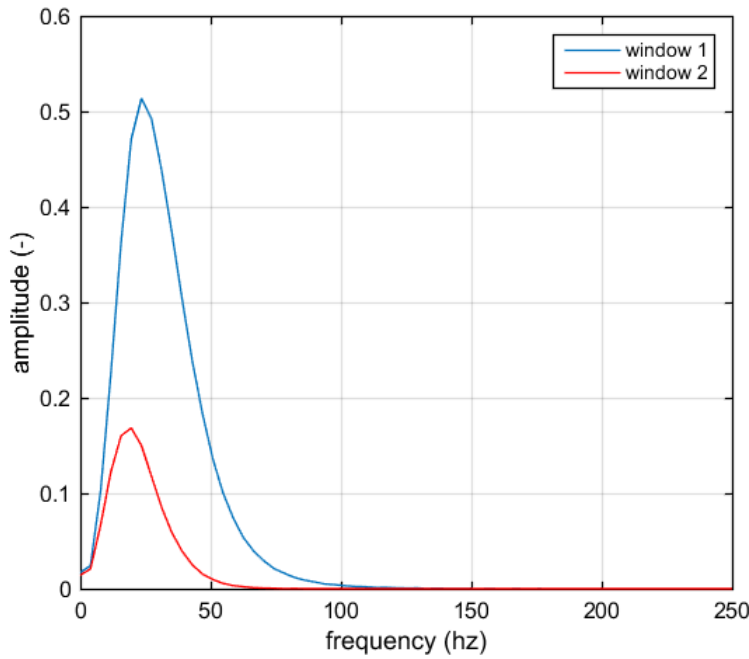
Figure 3.2. Amplitude spectra computed by taking the Fourier transform of a time window of 0.2 seconds about the upper (blue curve) and lower (red curve) reflections in Figure 3.1.
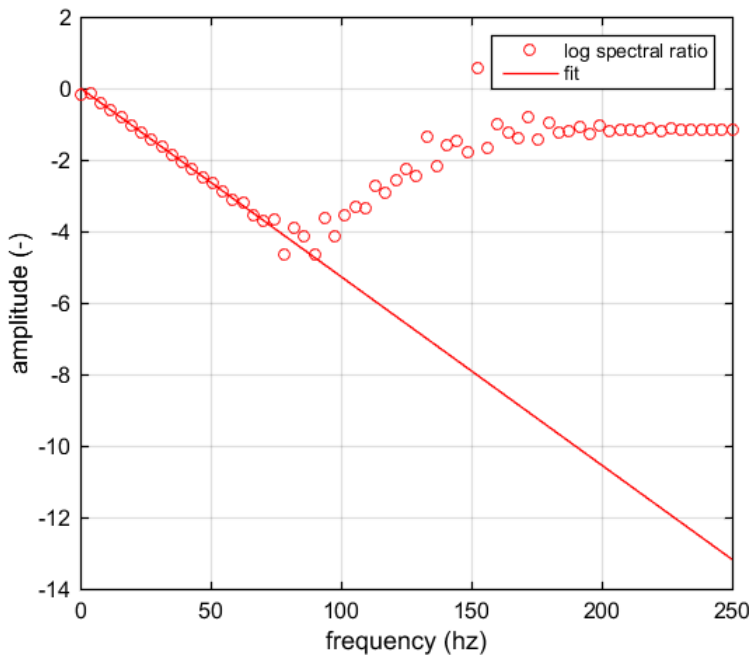
Figure 3.3. Log10 of the ratio between the two amplitude spectra shown in Figure . A linear regression (red line) has been fitted to the frequency range 0-70 Hz. The slope of this line can be used to compute Q using Equation 5.

Both Q estimation techniques are highly sensitive to random noise however (Figure 3.4). It is clear that stable estimates of Q require high signal-to-noise ratios (SNR), which means that

application to a real dataset will require careful selection of appropriate time windows to isolate high signal areas in the data.
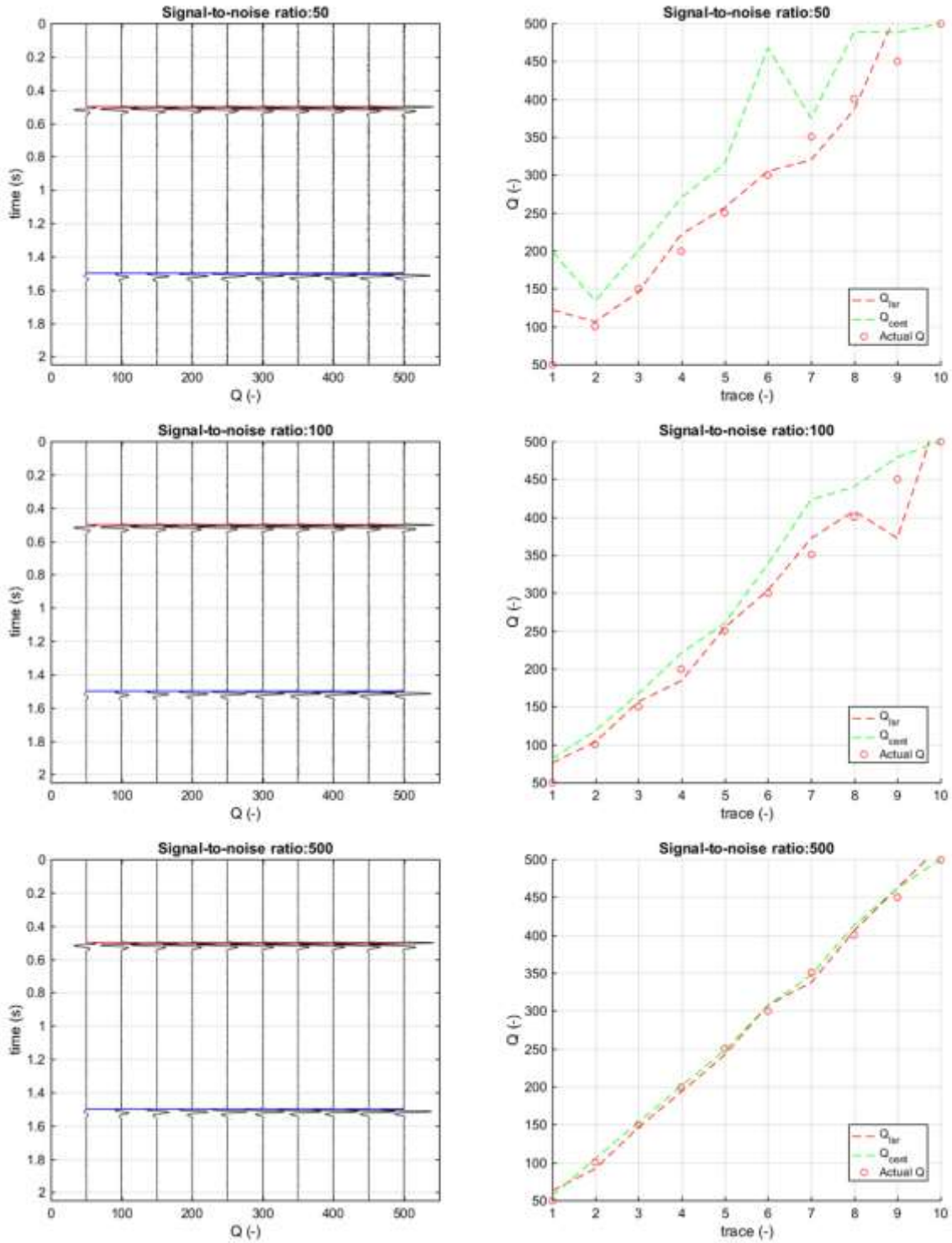
Figure 3.4. The effect of uncorrelated Gaussian white additive noise on Q estimation stability. Stable estimates of Q require high signal-to-noise ratios in order to form stable spectra for analysis.

13

3.6.2   Real data example

In order to demonstrate the workflow for Q estimation from stacked seismic data, a single inline from the 1999 Sleipner repeat seismic survey was analysed using a combination of the techniques described above. The seismic section (Figure 3.5) shows rather noisy traces, with the brightest reflections occurring in the CO_2 plume between traces 200 and 300. Scattered high amplitude reflections between 0.6 and .0.8 s travel time correspond to methane accumulations in the caprock.

Q analysis of the post-stack Sleipner data proved particularly challenging and was complicated by a number of factors:

1. Wavelet interference.
2. Energy from reflection multiples contaminating the reference spectra used to calculate Q.
3. Shallow gas accumulations above the reservoir, which cause signal scattering and attenuation in part of the data.
4. Time-dependent amplitude recovery applied during processing.
5. Deconvolution (spectral whitening) applied during processing.
6. Low SNR.

The SNR for each trace is plotted below the seismic section (Figure 3.5). The signal power was computed from the zero lag of the cross-correlation between neighbouring traces, while noise power was estimated from the zero lag of the average auto-correlation of the two traces, minus the signal estimate. This technique assumes that the signal component is the same between adjacent traces and the noise component is different and random. The mean SNR for the entire seismic line is around 12, with higher values approaching 30 in the vicinity of the CO_2 plume. Synthetic tests suggest that the data are not suitable for robust Q estimation (Figure 3.4), although it might be possible to achieve a meaningful measure of attenuation by carefully selecting suitable traces for analysis.

For this example, Q was estimated from the final stacked and migrated seismic data using frequency spectra extracted in narrow time windows about a reflection from close to the top of the Utsira Sand reservoir (Figure 3.5) and about a high amplitude regional reflector some distance below the Utsira reservoir (Figure 3.5). A narrow time window was essential for two reasons:

1. The low Signal-to-Noise Ratio (SNR) and lack of reflectivity at reservoir level means that reliable Q estimates require careful selection of appropriate time windows to isolate high signal areas in the data.

2. The CO_2 is trapped beneath a low permeability mudstone close to the top of the reservoir, so spectra used for Q estimation need to be selected from a short time window about this reflection.

To this end, the SPWVD time-frequency distribution described above was used to calculate frequency spectra. Q values were then calculated for traces 30, 273 and 480 (Figure 3.5) selected on the basis of SNR and observed reflection strength (Figures 3.6 to 3.8).
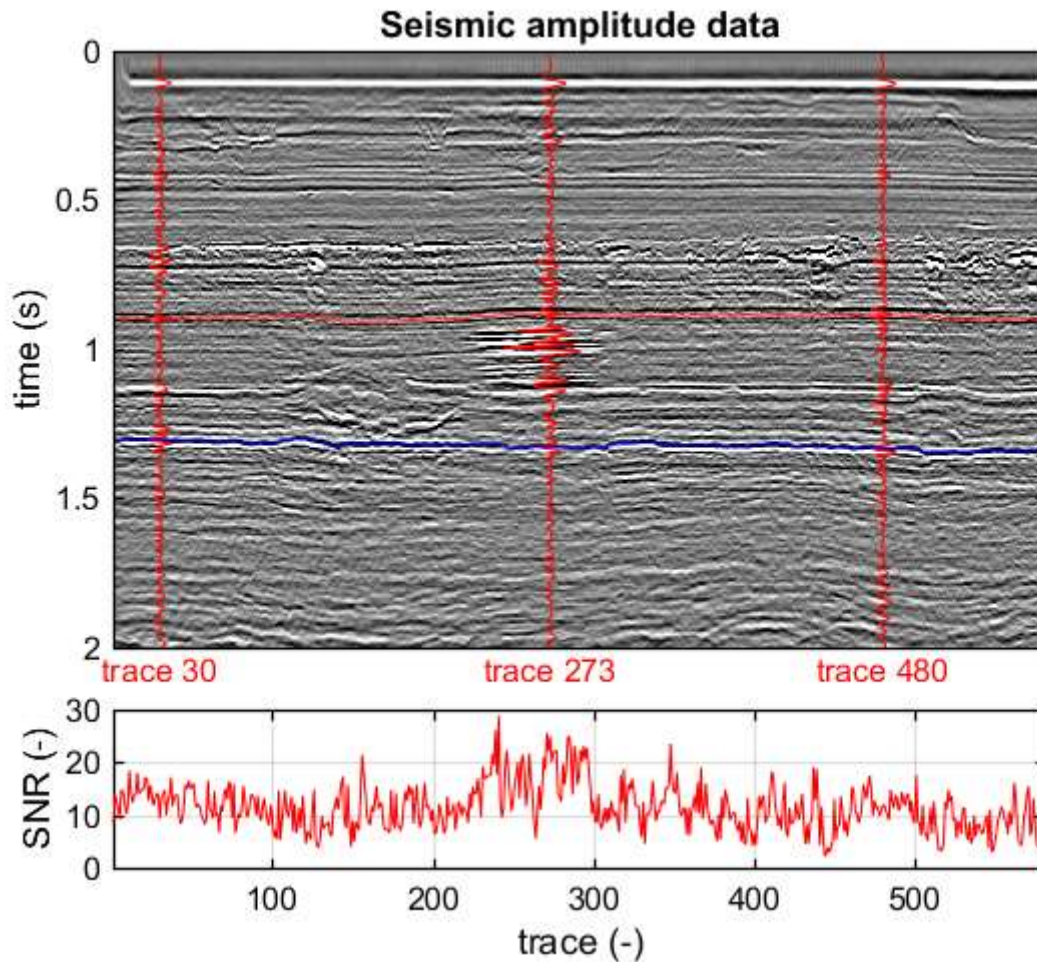
Figure 3.5. Seismic inline from the 1999 Sleipner monitor survey, showing the reflective CO_2 plume in the central part of the section. One reflector close to the top of the Utsira Sand (red line) and one some distance below the Utsira Sand (blue) were used to estimate Q with analysed traces shown as red wiggle traces. Lower panel shows a signal-to-noise estimate computed on a trace-by-trace basis. The mean signal-to-noise ratio is around 12.

Figure 3.6. Q analysis of Trace 30 on the seismic section in Figure 3.5, outside the CO₂ plume. (a) The extracted seismic trace. (b) Time-frequency decomposition using the SPWVD. (c) Smoothed frequency spectra extracted from the data. (d) Log spectral ratio plot showing the straight line fit used to calculate Q. Red and blue stippled lines in (a), (b) and (c) show the time picks used in the Q analysis.
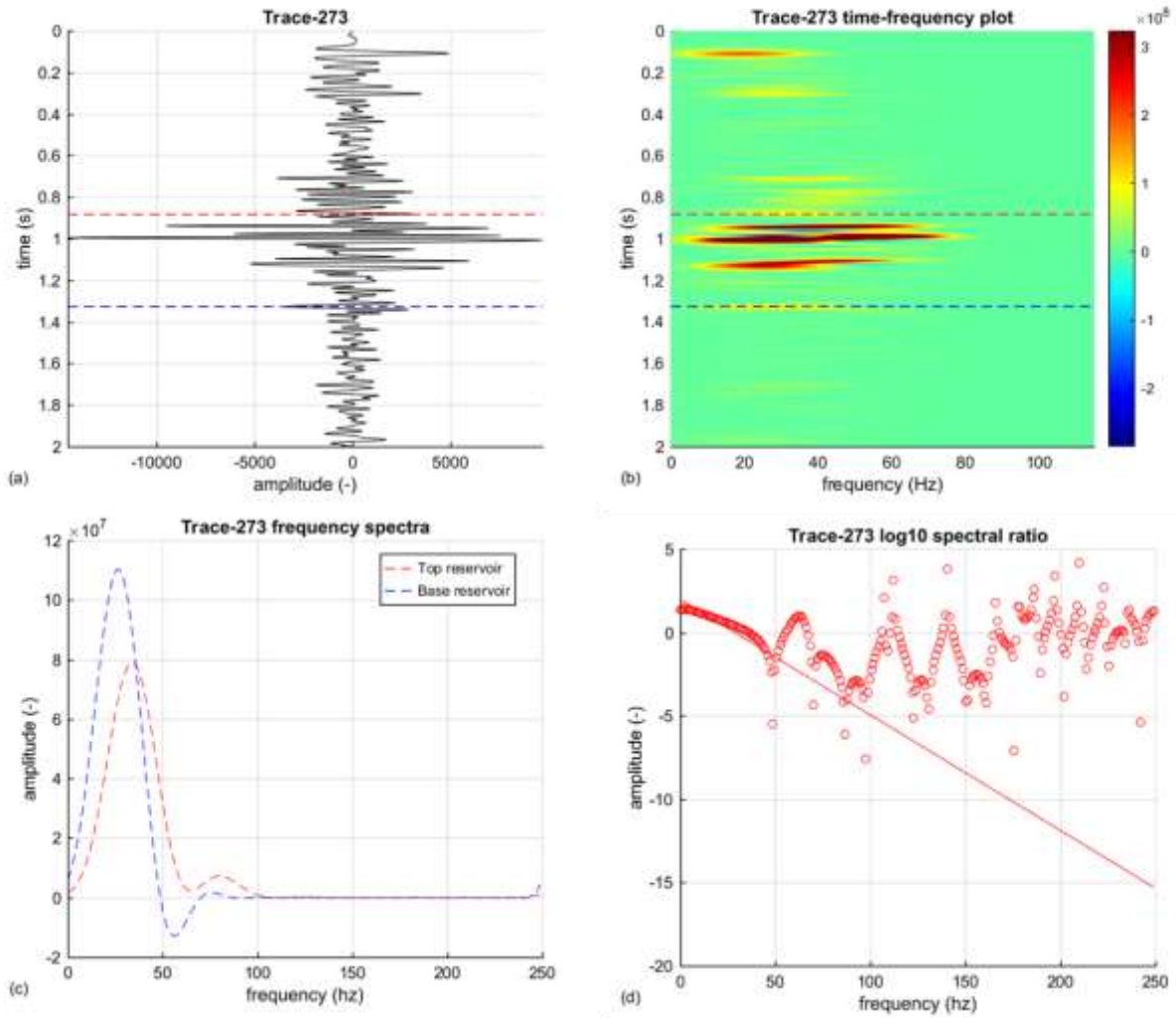
Figure 3.7. Q analysis of Trace 273 on the seismic section in Figure 3.5, located within the CO_2 plume. (a) The extracted seismic trace. (b) Time-frequency decomposition using the SPWVD. (c) Smoothed frequency spectra extracted from the data. (d) Log spectral ratio plot showing the straight line fit used to calculate Q. Red and blue stippled lines in (a), (b)and (c) show the time picks used in the Q analysis.

17
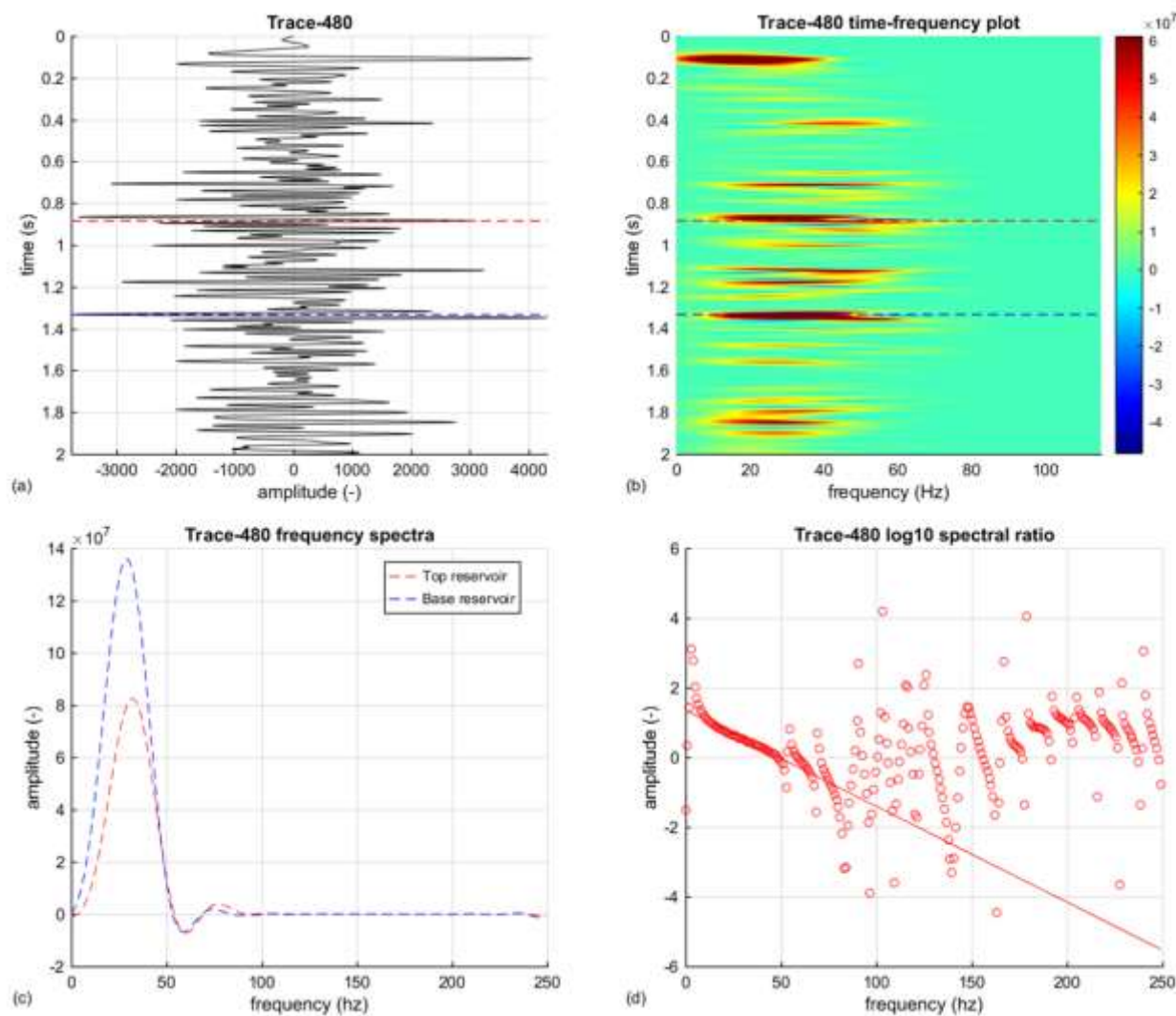
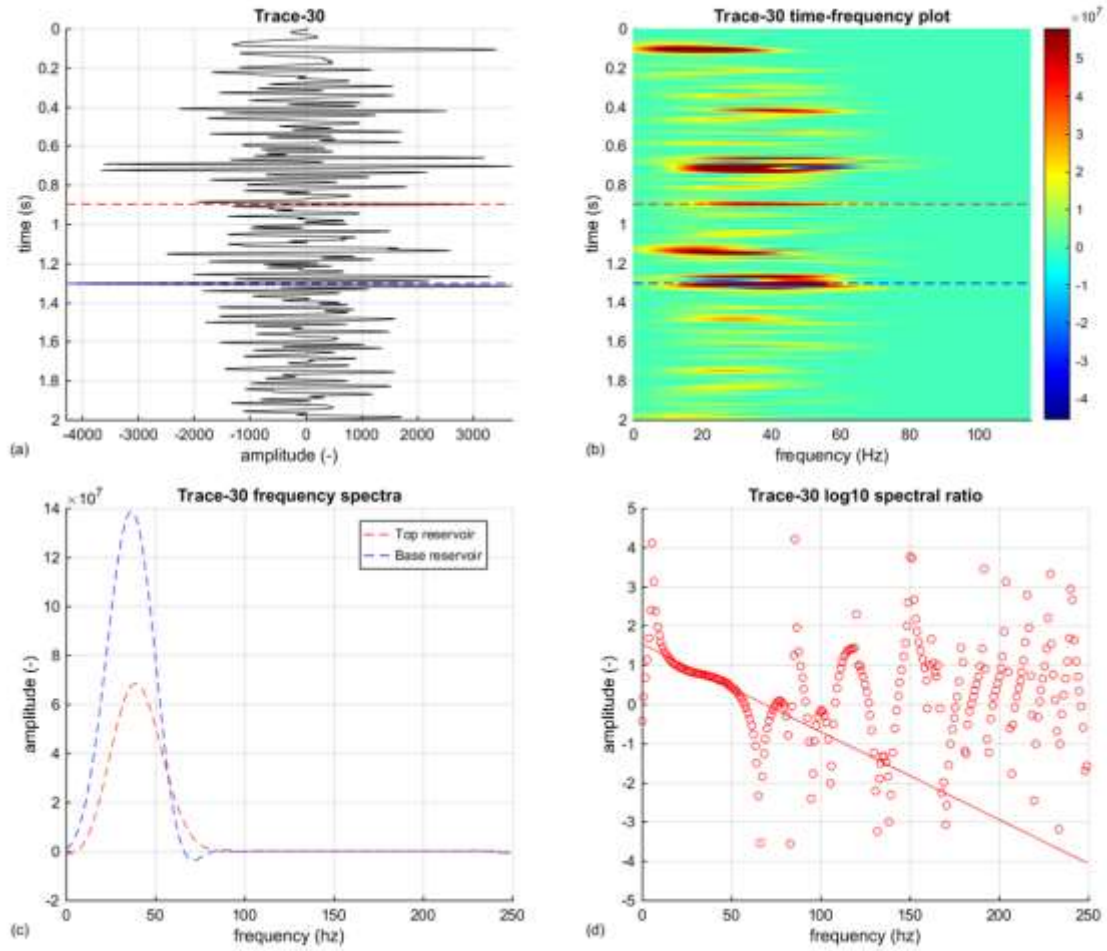*Figure 3.8. Q analysis of Trace 480 on the seismic section in Figure 3.5, from outside the CO₂ plume. (a) The extracted seismic trace. (b) Time-frequency decomposition using the SPWVD. (c) Smoothed frequency spectra extracted from the data. (d) Log spectral ratio plot showing the straight line fit used to calculate Q. Red and blue stippled lines in (a), (b) and (c) show the time picks used in the Q analysis.*

Calculated Q values (Table 3.1) can be compared with laboratory measurements on an Utsira Sand core sample made by Falcon-Suarez et al. (2018) as part of DISECCS. They found that the P-wave attenuation ($1/Q_P$) in partially saturated rock increased from 0.02 - 0.03 (Q = 50 - 32) in brine saturated rock to around 0.06 - 0.08 (Q = 17 - 12.5). New rock physics relationships proposed by Falcon-Suarez et al. (2018) indicate that at higher CO_2 saturations (80% and above) Q values would be in the range 20-30. There is therefore a degree of agreement on these figures. Traces 30 and 480, through the brine-filled reservoir, have high Q values, similar to the laboratory measurements. Trace 273, through the CO_2 plume has lower Q values, but consistent with generally quite high CO_2 saturations.

Trace	Q_{LSR}	Q_{PFS}	Q_{MEAN}	$1/Q_{MEAN}$
30	56.97	66.00	61.45	0.0163
273	19.26	28.00	23.63	0.0423
480	51.35	55.00	53.18	0.0188

Table 3.1. Results of Q analysis on selected traces extracted from the seismic line in Figure . LSR log spectral ratio; PFS peak frequency shift.

Automated analysis of the entire seismic section proved less successful, with many traces giving highly unstable Q estimates. It might be possible to improve the results by re-processing selected traces using a scheme designed to more accurately preserve amplitude information inherent in the signal. Noise could potentially be attenuated by forming "super-gathers" of adjacent common midpoint bins.

3.7   REFERENCES

Falcon-Suarez, I., Papageorgiou, G., Chadwick, A., North, L., Best, A. & Chapman, M. 2018. CO_2-brine flow-through on an Utsira Sand core sample: experimental and modelling. Implications for the Sleipner storage field. International Journal of Greenhouse Gas Control, 68 (2018), 236-246.

Zhang, C. & Ulrychz, T.J., 2002. Estimation of quality factors from CMP records. Geophysics 1542–1547.

4 Fracture properties from seismic coda analysis

4.1 BACKGROUND

The occurrence and characteristics of fracturing in reservoirs and overburdens is a key storage performance issue. Multi-component seismic data are typically used to characterise structural anisotropy, but a logistically simpler approach involves the use of conventional 3D or multi-azimuth 2D datasets. As a seismic wave propagates through the fractured medium the wavelet is lengthened by a reverberating or ringing 'coda' or tail. Coda development is most pronounced where the direction of propagation is parallel to the fracture system. So in principle the fracture direction can be determined by analysing the length of the ringing 'coda' for seismic lines acquired along different azimuths.

4.2 THEORY

Willis et al. (2006) described an algorithm to extract fracture distribution and orientation from scattered seismic coda, where the fracture spacing is of a comparable dimension to the wavelength of the seismic wavelet. Their algorithm was based on synthetic seismic models of a simple reservoir comprising five layers of homogenous isotropic elastic media. A series of anisotropic vertical fractures were introduced in the third layer of the model and assigned an elastic stiffness of 8×10^8 Pa m^{-1}, to represent gas-filled fractures. Synthetic shot records were generated for a series of models with fractures spaced at 10, 25, 35, 50 and 100 metres.

It was found that reflections beneath the fracture zone exhibited a ringing coda caused by reverberations in the fractured zone. However a shot record acquired normal to the fracture direction had little coherent energy below the top of the fractured zone, whereas shot records acquired parallel to the fractures showed coherent reflections from below the top fractured zone reflection. Consequently, the strike of the fracture zone could be identified using stacked NMO-corrected azimuthal gathers.

In order to apply coda analysis to real datasets, the authors computed a transfer function by deconvolving the autocorrelation function computed in a window above the fractured zone from the autocorrelation function computed in a window below the fractured zone, using the Wiener-Levinson algorithm. A clean spike or pulsed transfer function indicates no scattering, whereas a long, ringing, transfer function is indicative of scattering within the zone between the two analysis windows. The transfer functions from traces stacked in the direction parallel to fractures exhibited more ringing than those in the direction perpendicular to fractures, albeit with transfer functions showing very little change in shape until they were within 10° of the fracture strike direction on the synthetic test examples.

Willis et al. (2006) defined a scattering index (SI) to quantify the amount of ringing in the transfer function (t_i) of the form:

$$SI = \sum_{i=0}^{m} |t_i| \, i^n \qquad\qquad\qquad \text{Equation 7}$$

Where i is the time lag, n is an exponent equal to unity and m represents the lag at which the energy of the transfer function is insignificant.

The scattering index is largest in the fracture-parallel direction. The program *dsucoda* computes this scattering index for seismic traces in CWPSU format.

4.3   ALGORITHM

1. Read the CWPSU formatted seismic trace data and window about two time picks above and below the zone of interest.
2. Compute the autocorrelations of the windowed trace data.
3. Form the transfer function using the Wiener-Levinson deconvolution algorithm (Levinson recursion to solve the Toeplitz matrix).
4. Output the resulting transfer function in CWPSU trace format.
5. Compute the scattering index using Equation 7.

4.4   IMPLEMENTATION

The scattering index described above can be computed using *dsucoda*, which is contained in the *coda* directory of the DiSECCS toolbox. It has been implemented in ANSI C as a plug-in to the freely available Seismic Unix seismic data processing toolkit (http://www.cwp.mines.edu/cwpcodes/).

4.5   EXAMPLE USAGE

Willis et al. (2006) presented an example of coda analysis applied to a 3D seismic survey acquired over a fractured carbonate hydrocarbon reservoir (the Emilio field) in the central part of the Adriatic Sea, near the eastern coast of Italy. This technique clearly has the potential to enhance seismic monitoring of fractured CO_2 storage reservoirs.

4.6   REFERENCES

Willis, M.E., D.R. Burns, R. Rao, B. Minsley, M.N. Toksöz & L.Vetri. 2006. Spatial Orientation and Distribution of Reservoir Fractures from Scattered Seismic Energy. Geophysics 71 (5): O43. doi:10.1190/1.2235977.

5 Spectral inversion

5.1   BACKGROUND

Spectral inversion is a technique that uses spectral decomposition to improve characterisation of layers below the seismic tuning thickness. Absolute temporal layer thickness can be determined together with the reflection coefficients of the upper and lower layer interfaces which can be used to constrain layer velocity.

5.2   THEORY

The spectral inversion technique contained in the DiSECCS toolbox uses an inversion algorithm formulated in the frequency domain. The method for two reflections is based on the constant periodicity of the amplitude spectrum for a single layer of thickness T. The cost function is defined by Puryear & Castagna (2008) as:

$$cost\ function = G(f)\frac{dG(f)}{df} + 2\pi Tk\sin(2\pi fT)$$

Equation 8

It is evaluated across a range of frequencies. $G(f)$ is the magnitude of the amplitude spectrum and $k = r_e^2 - r_o^2$ where r_o and r_e are the odd and even components of the reflection coefficient pair. Finding the global minimum of the cost function by scanning a reasonable model space in T and k gives the desired solution for T and k. The remaining parameters are then calculated from:

$$r_o = \sqrt{\frac{G(f)^2}{4} - k(\cos(\pi fT))^2}$$

Equation 9

And

$$r_e = \sqrt{k - r_o^2}$$

Equation 10

5.3   ALGORITHM

1. Read in the seismic trace and source wavelet and transform both trace and wavelet into the frequency domain.
2. Calculate the normalised amplitude of the input trace at discrete frequency values.
3. Calculate the gradient of the amplitude distribution in the frequency domain.
4. Estimate the cost function across a suitable frequency range to determine the temporal thickness of the layer, T, and k.
5. Loop through the selected frequency range and derive the odd and even components of the reflection amplitude pair.
6. Output results.

5.4   IMPLEMENTATION

The spectral inversion algorithm described above has been implemented in the ANSI C code *dsuspecinv2*, which is included in the *specdecomp* directory of the DiSECCS toolbox. This is a plug-in to the freely available Seismic Unix seismic data processing toolkit (http://www.cwp.mines.edu/cwpcodes/) and the input data comprise seismic trace(s) in CWPSU format. Output from the code consists of two text files containing the calculated reflectivity response and the evaluated cost function. Note that *dsuspecinv2* uses the Fast Fourier Transform package FFTW3 which can be downloaded from www.fftw.org.

5.5   EXAMPLE USAGE

5.5.1   Synthetic example

A simple synthetic example of a seismic trace containing two reflections is shown in Figure 5.1. The top reflection coefficient is -0.2, the bottom reflection coefficient is 0.1 and the layer spacing is 8 milliseconds. The reflectivity series has been convolved with a Ricker wavelet with a peak frequency of 30 Hz. The cost function (Figure 5.2) clearly shows a global minimum at k=-0.02 and T=0.08 s.
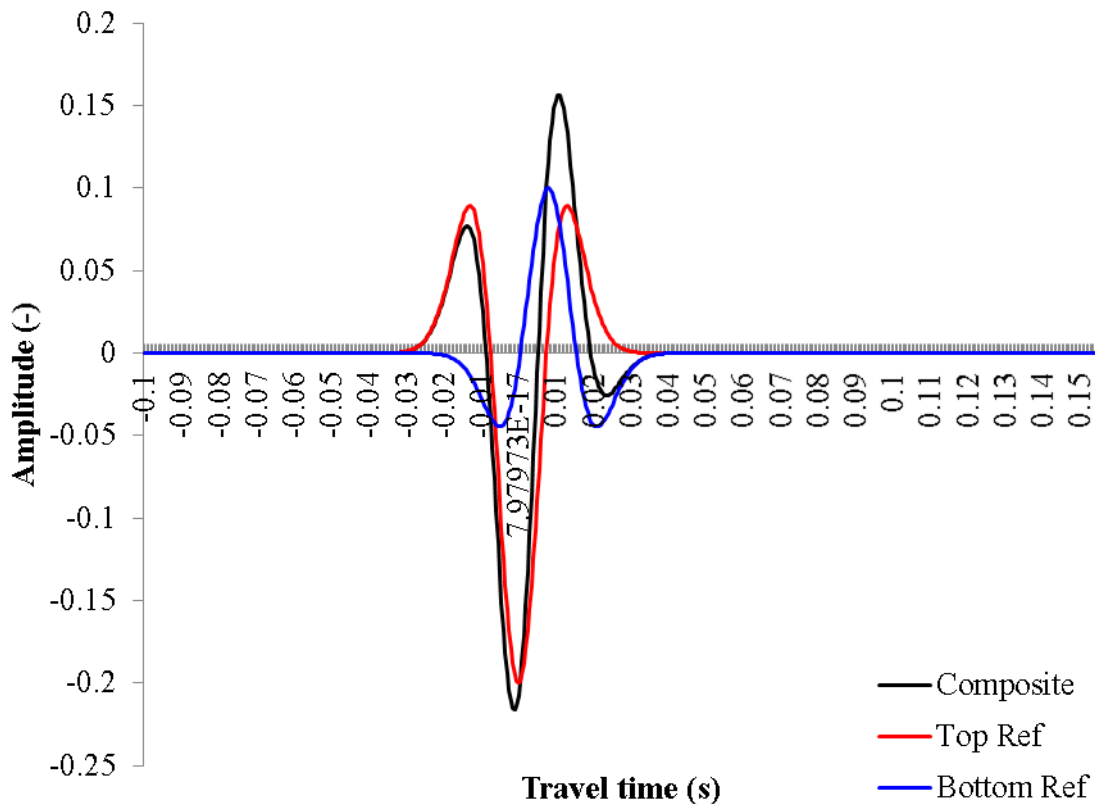

Figure 5.1. Top (red line) and base (blue line) reflections and the composite seismic trace resulting from the superposition of the two reflections (black line).
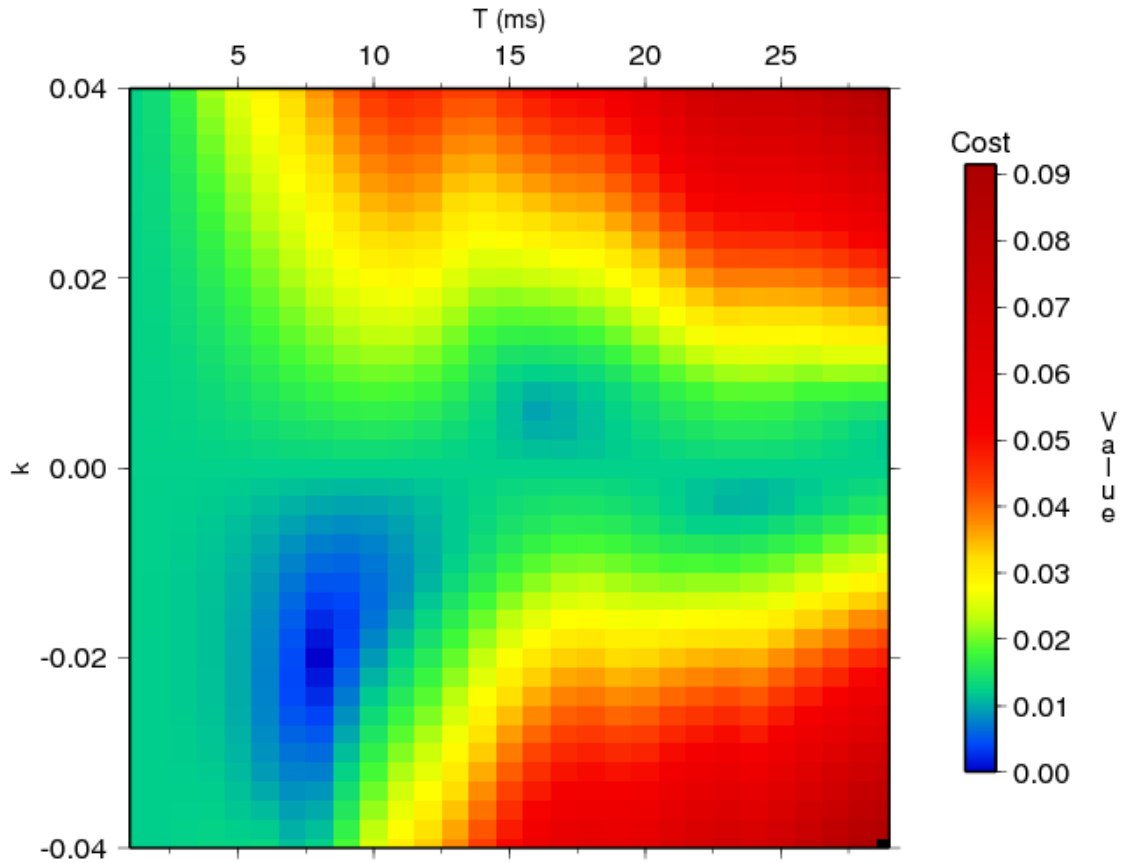
23

Figure 5.2. Cost function in k and T space. The cost function shows a global minimum at k=-0.02 and T=0.08 s.

5.5.2 Real example

The technique has been applied to a thin CO_2 layer within the Sleipner plume with mixed results (White et al., 2013). The lack of resolution for real data is a consequence of the difficulty in isolating a clean wavelet from a layer reflection amplitude pair which does not suffer interference effects from overlying and underlying reflectivity.

5.6 REFERENCES

Puryear, C.I. & Castagna, J.P. 2008. Layer-thickness determination and stratigraphic interpretation using spectral inversion: Theory and application. Geophysics 73 (2), R37-R48.

White, J.C.,Williams, G.A. & Chadwick, R.A. 2013. Thin Layer Detectability in a Growing CO_2 Plume: testing the Limits of Time-lapse Seismic Resolution. Energy Procedia 37, 4356–4365. doi:10.1016/j.egypro.2013.06.338

6 Rock Physics Models

6.1   BACKGROUND

Robust interpretation and analysis of seismic datasets must be underpinned by good understanding of the physical processes that govern the seismic properties of reservoir rock as fluid and stress distributions change.

6.2   IMPLEMENTATION

The rock physics models are implemented as a *Mathematica* note book (*DiSECCS_rock_physics_models.nb*) included in the *.mathematica* directory of the DiSECCS toolbox. A free viewer can be downloaded from the URL: http://www.wolfram.com/cdf-player

6.3   INPUT PARAMETERS

The two rock physics models are based on a Squirt-flow model described in Chapman et al. (2002) and Chapman (2003). These models require the user to input a series of parameters describing the elastic properties of the rock matrix and the fluid inclusions (in this case formation brine and CO_2). Example parameters for the Utsira Sand reservoir and caprock at the Sleipner injection operation are shown in Table 6.1 and 6.2, with CO_2 and brine fluid properties in Figure 6.1.

Variable	Utsira Sand	Caprock	Units	Description
KMineral	40×10^9	20×10^9	Pa	Grain bulk modulus
muGrain	20×10^9	10×10^9	Pa	Grain shear modulus
KDry	1.4×10^9	5.0×10^9	Pa	Dry frame bulk modulus
phi	0.37	0.2	-	Porosity
k	1.0×10^{-11}	1.0×10^{-15}	M^2	Absolute permeability
RhoSolid	2650.0	2650.0	Kg/m^3	Matrix density
muMatrix	0.83×10^9	1.0×10^{10}	Pa	Dry frame shear modulus
AspectRatio	1.0×10^{-4}	1.0×10^{-4}	-	Crack aspect ratio
CrackDensity	0.01	0.01	-	Crack density
CharFreq	50.0	50.0	-	Effective time scale

Table 6.1. Elastic properties of the Utsira Sand reservoir and its caprock at the Sleipner CO_2 injection site, for input into the rock physics models described below.

Variable	CO_2	Brine	Units	Description
K	7.9×10^7	2.4×10^9	Pa	Bulk modulus
eta	6.1×10^{-5}	6.0×10^{-4}	Pa.S	Viscosity
Rho	7.4×10^2	1.0×10^3	Kg/m^3	Density

Table 6.2. Fluid properties for brine and CO_2 at 28 °C and 8 MPa, for input into the rock physics models described below.
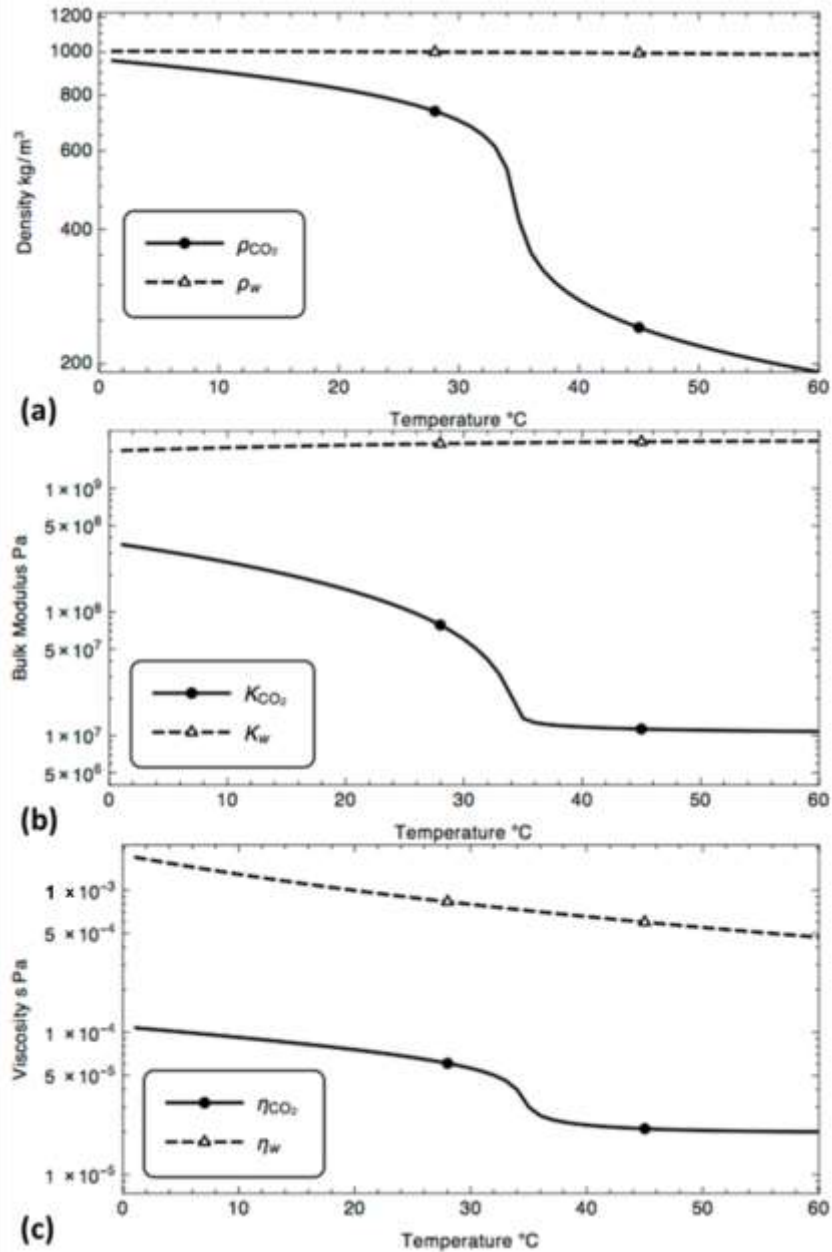
Figure 6.1. Fluid properties for CO_2 and brine (w) at a pressure of 8 MPa. (a) Density ρ; (b) bulk modulus K and (c) viscosity η.

6.4 DETERMINING EFFECTIVE FLUID MODULUS IN A CRACKED POROUS MEDIUM

The algorithms are based on a Squirt-flow model described in Chapman et al. (2002), Chapman (2003) and Papageorgiou & Chapman (2015), in which the grains of a porous material are themselves allowed to have porosity in the form of micro-cracks. The effective fluid moduli are computed by assuming that fluids are distributed between pores (S_p) and cracks (S_c) in the rock:

$$S_p = \begin{cases} S_w \frac{1-c_f/S_0}{1-c_f}, & S_w < S_0 \\ \frac{S_w-c_f}{1-c_f} & S_w > S_0 \end{cases} \qquad S_c = \begin{cases} S_w/S_0, & S_w < S_0 \\ 1 & S_w > S_0 \end{cases}$$

Equation 11

Where Sw is the water saturation, S_0 is a critical saturation parameter and c_f is given by:

$$c_f = \frac{\frac{4}{3}\pi\epsilon r}{\frac{4}{3}\pi\epsilon r + \phi}$$

Equation 12

Where ε is the crack density and r the aspect ratio of the cracks. The cracks are modelled as coin-like ellipsoidal inclusions with a crack density (ε) given by $\varepsilon = \frac{3\varphi_c}{4\pi r}$ where φ_c is the volume fraction of cracks in the effective medium.

Pores and cracks are assigned different fluid moduli in the model as illustrated by the example pseudocode (Box 6.1). This formulation incorporates hysteresis effects, as the spatial distribution of fluids between cracks and pores will be different during imbibition and drainage (see Papageorgiou & Chapman 2015 for a detailed explanation).

```
/* input */
Phi /*porosity */
AspectRatio /* crack aspect ratio */
CrackDensity /* crack density */
waterModulus /* brine bulk modulus */
gasModulus /* CO2 bulk modulus */

/* calculate crack fraction */
crackFraction=(4/3*pi*CrackDensity*AspectRatio)
/(4/3*pi*CrackDensity*AspectRatio + phi)

/* calculate relative saturations */
If (0 < Sw < S0)
     Sp=Sw((1-cf/S0)/1-cf))
     Sc=Sw/S0
Else If (S0 < Sw < 1)
     Sp=(Sw -cf)/1-cf)
     Sc=1

/* Output fluid moduli for pores and cracks */
CrackFluidModulus=1(Sc/waterModulus+1-Sc)/gasModulus)
PoreFluidModulus=1(Sp/waterModulus+1-Sp)/gasModulus)
```

Box 6.1. Pseudo-code showing calculation of effective fluid moduli for use in the rock physics models described below. Input parameters are shown in red and are defined in Table 6.1 and 6.2. Output parameters are highlighted in blue.

6.5   THE EFFECT OF CAPILLARY PRESSURE ON THE EFFECTIVE FLUID MODULUS

Papageorgiou et al. (2016) incorporated capillary pressure effects into their calculations of the effective fluid modulus by including a capillary pressure parameter q which relates the wetting and non-wetting phase fluid pressures:

$$\Delta P_{CO_2} = q\Delta P_w, \frac{K_{CO_2}}{K_w} < q < 1$$

Equation 13

Where P_{CO2} is the CO_2 (non-wetting phase) pressure, P_w the brine (wetting phase) pressure, K_{CO2} the CO_2 bulk modulus, and K_W the brine bulk modulus.

The effective fluid modulus (Kf) is then calculated by:

$$\frac{1}{K_f} = \frac{1}{S_w(1-q)+q}\left(\frac{S_w}{K_w} + q\frac{1-S_w}{K_{CO_2}}\right)$$

Equation 14

Where S_W is the brine saturation.

Example pseudocode used to calculate $K_{f is}$ shown in Box 6.26.2, while Figure 6.2 shows the effect on fluid bulk modulus of varying the parameter q.

```
/* input */
Sw /*water saturation */
waterModulus /* brine bulk modulus */
gasModulus /* CO₂ bulk modulus */
q /* the q factor */

/* Output fluid modulus */
FluidModulus=…
 (Sw (1-q)+q)/(Sw/waterModulus+q*(1-Sw)/gasModulus)
```

Box 6.2. Pseudo-code showing calculation of effective fluid moduli incorporating capillary pressure effects for use in rock physics model 2 described below. Input parameters are shown in red and are defined in Table 6.1 and Table 6.2. Output parameters are highlighted in blue.
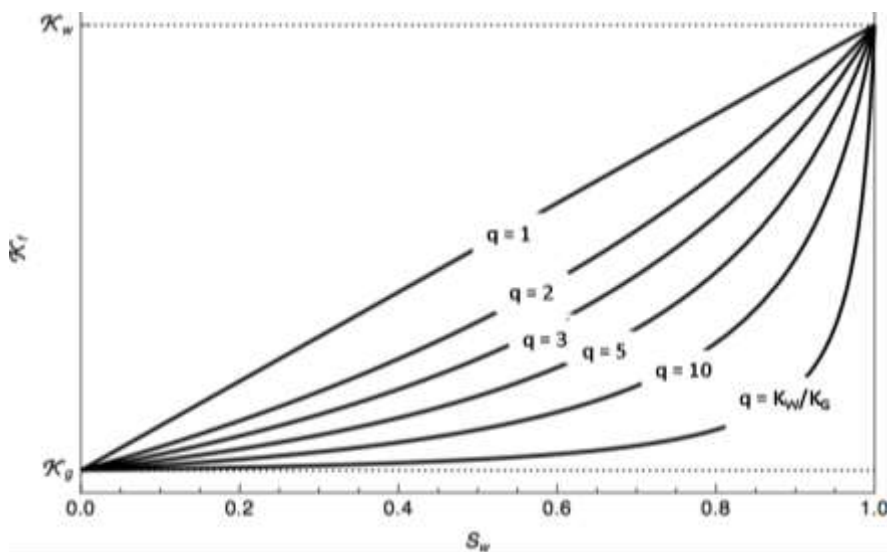

Figure 6.2. The effect of varying the capillary pressure parameter q on the effective fluid modulus (K_f).

6.6   THE EFFECTIVE TIMESCALE PARAMETER

Squirt-flow models introduce stiffening in the saturated rock matrix, based on a relaxation mechanism whose characteristic frequency depends on fluid content as well as rock matrix parameters. Chapman (2003) showed that fluid mobility is the key parameter affecting the characteristic time scale of this process, a fact that has been verified experimentally many times. The characteristic frequency (ω) of squirt flow is given by:

$$\omega \; = \; \frac{2\,\pi}{\tau} = \frac{B}{(1-q)\,Sw + q} \left(\frac{k_w}{\eta_w} + q\,\frac{k_{CO2}}{\eta_{CO2}} \right) \qquad\qquad \text{Equation 15}$$

Where τ is the characteristic time scale, the coefficient B is a function of various rock properties (around 50 Pa for the Utsira Sand), S_W is the water saturation, q as described above and k/η is the mobility of the effective fluid phase (relative phase permeability / phase viscosity).

Combining relative permeability measurements for the Utsira Sand (Figure 6.3) with the fluid properties in Table 6.2 and Figure 6.1, it is evident that the characteristic frequency for squirt flow in the Utsira Sand lies just above the typical time-lapse seismic band at around 100 Hz (Figure 6.4).
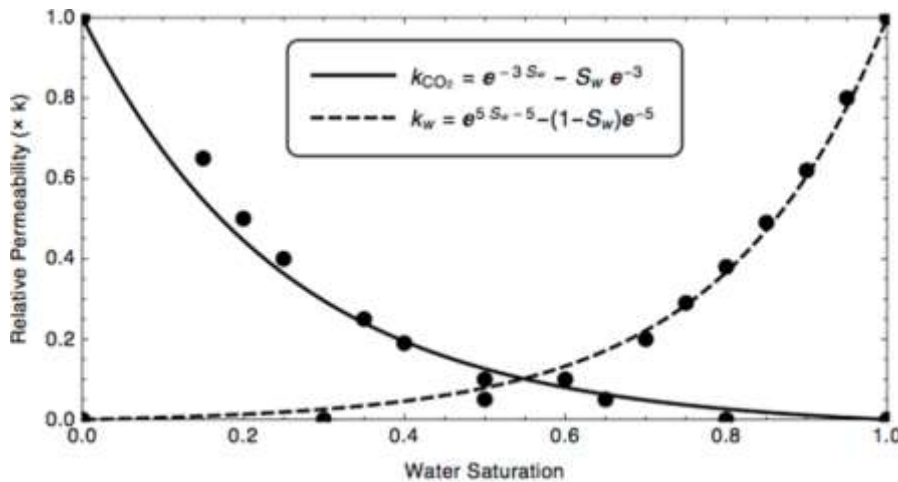

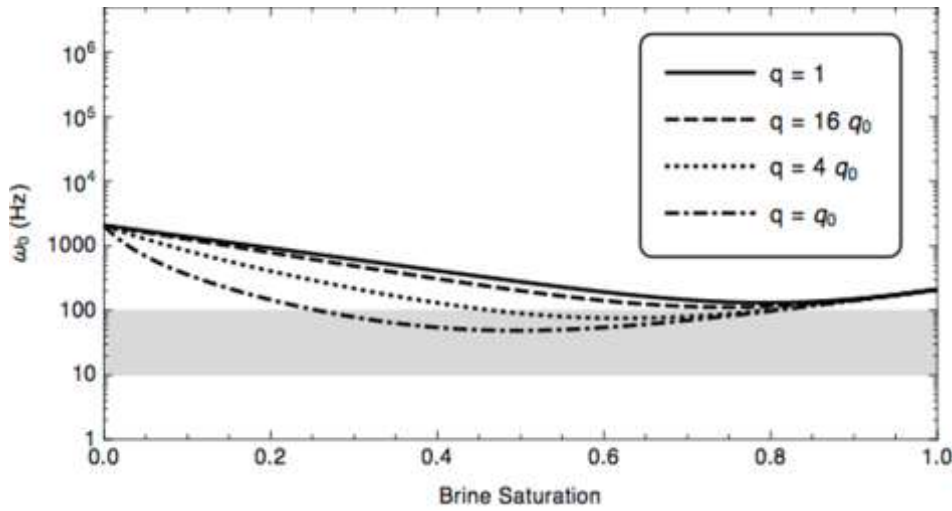*Figure 6.3. Relative permeability of CO_2 and brine in the Utsira Sand*

Figure 6.4. Characteristic frequency (ω_0) as a function of capillary pressure parameter (q) and brine saturation.

6.7   MODEL 1

6.7.1   Theory

The theoretical background to the model is described in Papageorgiou & Chapman (2015), which presents a generalized squirt flow model for two fluids, neglecting capillary pressure effects. Their model allows the calculation of effective fluid bulk modulus for use in rock physics analysis of the brine-CO_2 system.

6.7.2   Algorithm

Example pseudocode used to calculate the bulk modulus is shown in Box 6.2. Inputs to the algorithm are contained in Table 6.1 and 6.2 and include the elastic properties of the rock matrix, pore fluids and the characteristic frequency (ω) of squirt flow. An example output is shown in Figure 6.5.
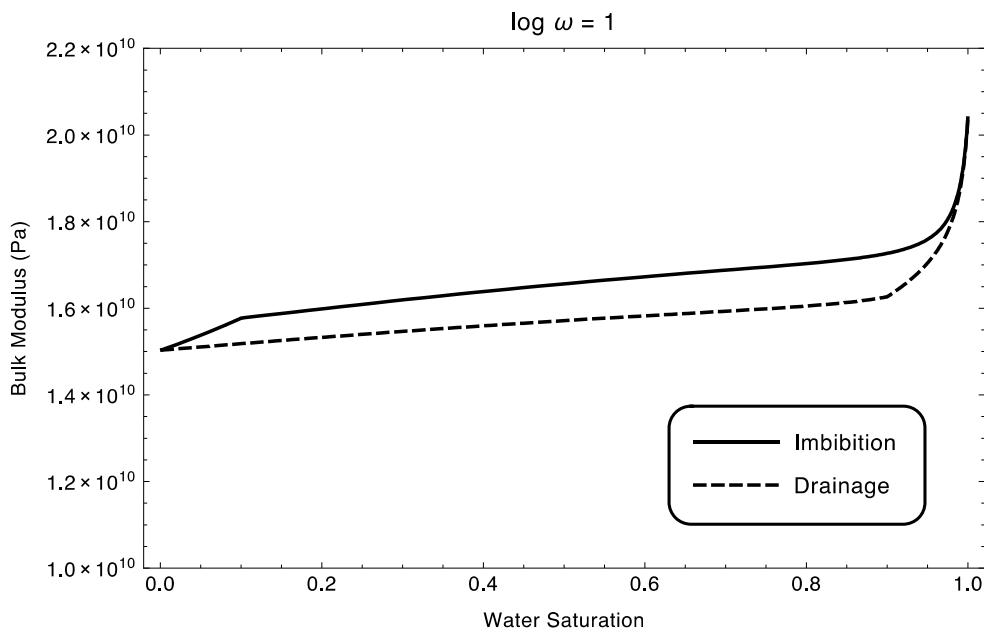

Figure 6.5. Bulk modulus versus saturation relationship for Model 1.

30

```
/* input: see Tables 2 and 3 */
KMineral, muGrain, KDry, Phi, phip, K, rhoSolid, muMatrix,
aspectRatio, crackDensity, CharFreq, K1, eta1, rho1, K2, eta2,
rho2, Sw, Sc, omega

/* Compute bulk rock density */
rho=(1-phi)*rhoSolid+phi*(Sw*rho1+(1-Sw)*rho2)

/* Compute Poisson's ratio */
nuGrain=(3*KMineral-2*muGrain)/(2*(3*KMineral+muGrain))

/* Compute Young's ratio */
lambdaGrain=KMineral-2*muGrain/3

/* Compute crack stiffness */
sigmac=(pi*muGrain*aspectRatio)/(2*(1-nuGrain))

/* Compute crack porosity */
phic=4*pi*crackDensity*aspectRatio/3

/* Compute fluid bulk moduli */
[CrackFluidModulus,PoreFluidModulus]=Function in Box1[Phi,
AspectRatio, CrackDensity, K1, K2]
Kp=(4*muGrain)/(3*PoreFluidModulus)
Kc=sigmac/CrackFluidModulus

/* Compute time-scale parameter */
tau=2*pi/ω0[K1, eta1, rho1, K2, eta2, rho2, Sw]

/* Intermediate calculations */
alpha=(1*i)*(phic*omega*tau)/sigmac
beta=(1*i)*(3*phip*omega*tau)/(4*muGrain)
A1=1+Kc
A2=1+Kp
B1=-KMineral
B2=-3*KMineral*(1-nuGrain)/(1+nuGrain)

/* Inclusion pressures solution in the frequency domain */
Pc=(beta*B2 + alpha*B1*(1+beta*A2))/(1-(1+alpha*A1)*(1+beta*A2))
Pp=(alpha*B1+beta*B2*(1+alpha*A1))/(1-(1+alpha*A1)*(1+beta*A2))

/* Output bulk modulus */
K=KDry+phic*(KMineral/sigmac+1) …
*Pc+phip*((3*KMineral)/(4*muGrain)+1)*Pp
```

*Box 6.2. Pseudo-code showing calculation of P-wave bulk modulus using rock physics Model 1.
Input parameters are shown in red and are defined in Table . Output parameters are highlighted
in blue.*

6.8   MODEL 2

6.8.1   Theory

The background to the model is described in Papageorgiou et al. (2016), which presents a theoretical derivation of a Brie-like fluid mixing law by incorporating a capillary pressure term into the inclusion-based model described above (see also Papageorgiou & Chapman 2015). The inclusions are saturated by multiple fluids.

6.8.2   Algorithm

Example pseudocode used to calculate the bulk modulus is shown in Box . Inputs to the algorithm are contained in Table 6.1 and 6.2. An example output is shown in Figure 6.6.
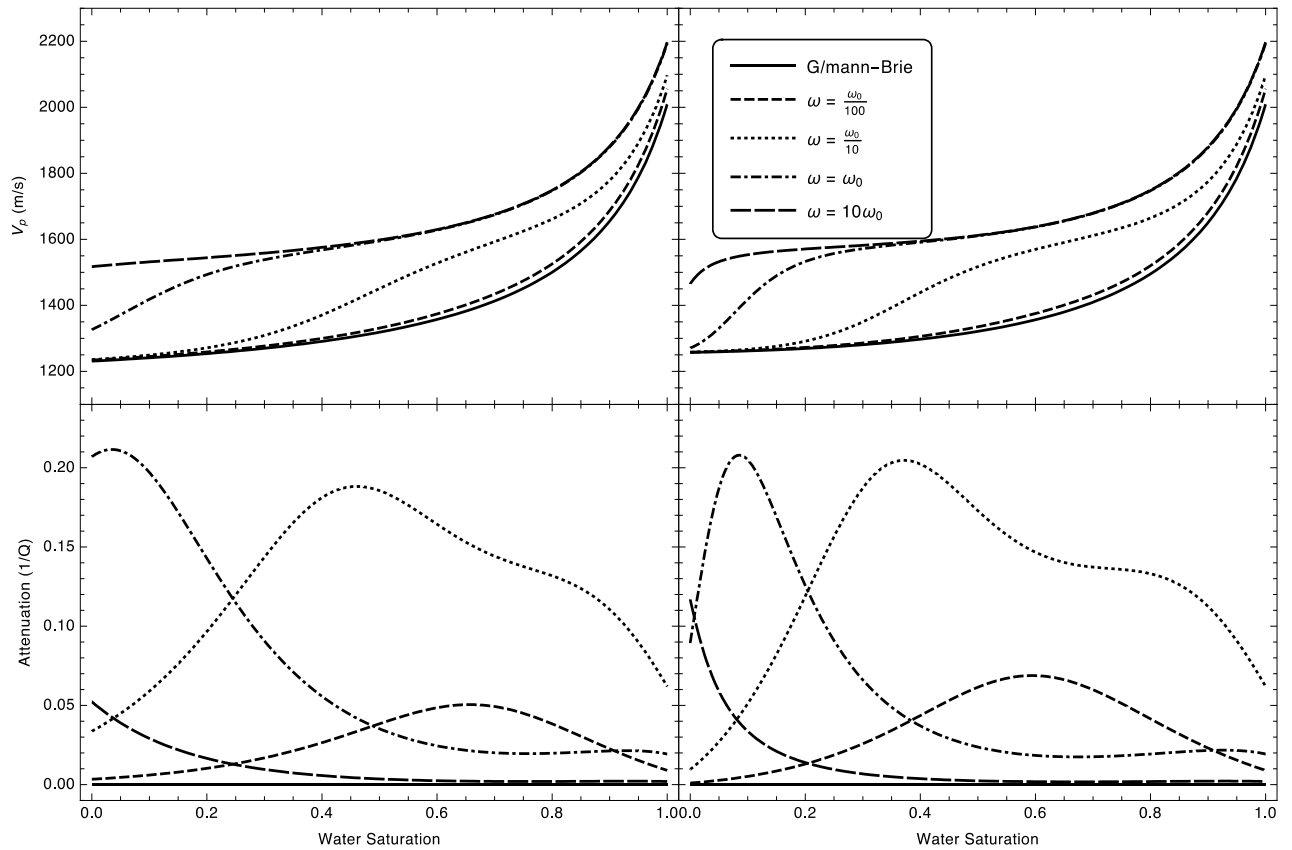

Figure 6.6. P-wave velocity (top) and attenuation (bottom) versus saturation relationship for Model 2 in the case of supercritical CO_2 (left) and liquid CO_2 (right) across different frequency ranges (ω).

```
/* input: see Tables 2 and 3 */
KMineral, muGrain, KDry, Phi, phip, K, rhoSolid, muMatrix,
aspectRatio, crackDensity, CharFreq, K1, eta1, rho1, K2, eta2,
rho2, Sw, Sc, omega

/* Compute bulk rock density */
rho=(1-phi)*rhoSolid+phi*(Sw*rho1+(1-Sw)*rho2)

/* Compute Poisson's ratio */
nuGrain=(3*KMineral-2*muGrain)/(2*(3*KMineral+muGrain))

/* Compute Young's ratio */
lambdaGrain=KMineral-2*muGrain/3

/* Compute crack stiffness */
sigmac=(pi*muGrain*aspectRatio)/(2*(1-nuGrain))

/* Compute crack porosity */
phic=4*pi*crackDensity*aspectRatio/3

/* Compute fluid bulk moduli */
[FluidBulkModulus]=Function in Box2[Sw, K1, K2, q]
Kp=(4*muGrain)/(3*FluidBulkModulus)
Kc=sigmac/FluidBulkModulus

/* Compute time-scale parameter */
tau=2*pi/ω0[K1, eta1, rho1, K2, eta2, rho2, Sw]

/* Intermediate calculations */
alpha=(1*i)*(phic*omega*tau)/sigmac
beta=(1*i)*(3*phip*omega*tau)/(4*muGrain)
A1=1+Kc
A2=1+Kp
B1=-KMineral
B2=-3*KMineral*(1-nuGrain)/(1+nuGrain)

/* Inclusion pressures solution in the frequency domain */
Pc=(beta*B2 + alpha*B1*(1+beta*A2))/(1-(1+alpha*A1)*(1+beta*A2))
Pp=(alpha*B1+beta*B2*(1+alpha*A1))/(1-(1+alpha*A1)*(1+beta*A2))

/* Output bulk modulus */
K=KDry+phic*(KMineral/sigmac+1) …
*Pc+phip*((3*KMineral)/(4*muGrain)+1)*Pp
```

Box 6.4. Pseudo-code showing calculation of P-wave bulk modulus using rock physics Model 2. Input parameters are shown in red and are defined in Table 6.1 and 6.2. Output parameters are highlighted in blue.

6.9   REFERENCES

Chapman, M. 2003. Frequency-Dependent Anisotropy due to Meso-Scale Fractures in the Presence of Equant Porosity. Geophysical Prospecting 51 (5): 369–79. doi:10.1046/j.1365-2478.2003.00384.x.

Chapman, Mk, S. V. Zatsepin & S. Crampin. 2002. Derivation of a Microstructural Poroelastic Model. Geophysical Journal International 151 (2): 427–51. doi:10.1046/j.1365-246X.2002.01769.x.

Papageorgiou, G. & M. Chapman. 2015. Multifluid Squirt Flow and Hysteresis Effects on the Bulk Modulus–water Saturation Relationship. Geophysical Journal International 203 (2): 814–17. doi:10.1093/gji/ggv333.

Papageorgiou, G., K. Amalokwu & M. Chapman. 2016. Theoretical Derivation of a Brie-like Fluid Mixing Law. Geophysical Prospecting 64 (4): 1048–53. doi:10.1111/1365-2478.12380.

7 Rock physics laboratory measurements

7.1 BACKGROUND

Direct measurement of rock samples in the laboratory provides the means of calibrating and verifying rock physics models such as those described above. Experimental work in DiSECCS focussed on unconsolidated sands such as are found at Sleipner and on synthetic rocks where properties in terms of porosity and permeability can to some extent be controlled.

7.2 METHODOLOGY

The experimental methodology can be found in the DiSECCS WP1 - 4 final report, with details of the experimental rig in Falcon-Suarez et al. (2014, 2016,2018).

7.3 RESULTS

An EXCEL spreadsheet containing measurements on a number of different samples, of P- and S-wave velocity, seismic attenuation and electrical resistivity are included in the *spreadsheets* directory of the DiSECCS Seismic Unix toolbox. Complete datasets of the experimental work developed during the project can be found on the UKCCSRC archive:
http://www.bgs.ac.uk/ukccs/dataset.cfm?id=19877273

7.4 REFERENCES

Falcon-Suarez, I., North, L. & Best, A. 2014. Experimental Rig to Improve the Geophysical and Geomechanical Understanding of CO_2 Reservoirs. European Geosciences Union General Assembly 2014, EGU Division Energy, Resources & the Environment (ERE) 59 (January): 75–81. doi:10.1016/j.egypro.2014.10.351.

Falcon-Suarez, I., North, L., Amalokwu, K. & Best, A. 2016. Integrated Geophysical and Hydromechanical Assessment for CO_2 Storage: Shallow Low Permeable Reservoir Sandstones. Geophysical Prospecting 64 (4): 828–47. doi:10.1111/1365-2478.12396.

Falcon-Suarez, I., Papageorgiou, G., Chadwick, A., North, L., Best, A. & Chapman, M. 2018. CO_2-brine flow-through on an Utsira Sand core sample: experimental and modelling. Implications for the Sleipner storage field. International Journal of Greenhouse Gas Control, 68 (2018), 236-246.